Naval Research Laboratory
Washington, DC 20375-5320

NRL/6350/MR—2023/3

Near Superhard Tungsten Carbide via Synergistic Nanostructural Features

KEVIN ANDERSON

JAMES WOLLMERSHAUSER

HEONJUNE RYOU

RAMASIS GOSWAMI

EDWARD GORZKOWSKI

Multifunctional Materials Branch
Materials Science and Technology Division

BORIS FEYGELSON

Power Electronics & Advanced Materials Branch
Electronics Science and Technology Division

December 28, 2023

REPORT DOCUMENTATION PAGE

Form Approved
OMB No. 0704-0188

1. REPORT DATE *(DD-MM-YYYY)*	**2. REPORT TYPE**	**3. DATES COVERED** *(From - To)*
28-12-2023	NRL Memorandum Report	12/6/2021 – 12/6/2022

4. TITLE AND SUBTITLE

Near Superhard Tungsten Carbide Via Synergistic Nanostructural Features

5a. CONTRACT NUMBER

5b. GRANT NUMBER

5c. PROGRAM ELEMENT NUMBER
NISE

6. AUTHOR(S)

Kevin P. Anderson, James A. Wollmershauser, Heonjune Ryou, Ramasis Goswami, Edward P. Gorzkowski, and Boris N. Feygelson

5d. PROJECT NUMBER

5e. TASK NUMBER

5f. WORK UNIT NUMBER
N20V

7. PERFORMING ORGANIZATION NAME(S) AND ADDRESS(ES)

Naval Research Laboratory
4555 Overlook Avenue, SW
Washington, DC 20375-5320

8. PERFORMING ORGANIZATION REPORT NUMBER

NRL/6350/MR--2023/3

9. SPONSORING / MONITORING AGENCY NAME(S) AND ADDRESS(ES)

Naval Research Laboratory
4555 Overlook Avenue, SW
Washington, DC 20375-5320

10. SPONSOR / MONITOR'S ACRONYM(S)

NRL-NISE

11. SPONSOR / MONITOR'S REPORT NUMBER(S)

12. DISTRIBUTION / AVAILABILITY STATEMENT

DISTRIBUTION STATEMENT A: Approved for public release; distribution is unlimited.

13. SUPPLEMENTARY NOTES

Karles Fellowship

14. ABSTRACT

Industrial application of superhard materials (Vickers hardness, HV > 40 GPa) such as diamond and cubic boron nitride is limited by high costs and complex routes of synthesis. However, recent efforts have demonstrated the potential for alternative materials with similar hardness via microstructural refinement. Though broadly utilized for its hardness, tungsten carbide (WC) falls well short of qualification as a superhard material even in its less common but harder binderless form (HV ~ 26 GPa). Despite recent advances in sintering technology, even the smallest grained binderless WC (< 100 nm) has failed to achieve HV values above 33 GPa. In this work, multiple hardening mechanisms are exploited through a unique sintering approach assisted sintering (EC-PAS) is utilized to produce fully dense, binderless nanocrystalline WC ceramics with HV as high as 39 GPa. The unprecedented WC hardness is attributed to the combined effects of record small grain size (26 nm) and nanoscale intragranular substructures resulting from lattice deformation observed through transmission electron microscopy (TEM). The demonstration of the superposition of multiple hardening mechanisms provides a potential generalized avenue to improve hardness of ceramics beyond traditional Hall-Petch methods, yielding new classes of superhard materials.

15. SUBJECT TERMS

Nanocrystalline, Superhard materials, Deformation structures
Sintering, EC-PAS

16. SECURITY CLASSIFICATION OF:			**17. LIMITATION OF ABSTRACT**	**18. NUMBER OF PAGES**	**19a. NAME OF RESPONSIBLE PERSON**
a. REPORT	**b. ABSTRACT**	**c. THIS PAGE**			Kevin P. Anderson
U	U	U	U	20	**19b. TELEPHONE NUMBER** *(include area code)* (202) 404-1512

Standard Form 298 (Rev. 8-98)
Prescribed by ANSI Std. Z39.18

This page intentionally left blank.

CONTENTS

This page intentionally left blank.

NEAR SUPERHARD TUNGSTEN CARBIDE VIA SYNERGISTIC NANOSTRUCTURAL FEATURES

1. INTRODUCTION

1.1 Superhard Materials

Superhard materials (Vickers hardness, *HV* > 40 GPa) represent the state-of-the-art for a variety of industrial applications including machining tools and abrasives. However, widespread adoption of these materials has been hindered by limited compositions requiring expensive and complex production processes. The few commonly known intrinsically superhard materials, such as diamond (*HV* 80-150 GPa [1,2]) and cubic boron nitride (cBN) (49 GPa [3,4]), attain hardness through atomic structure and interatomic bonding. Alternatively, extrinsically superhard materials achieve hardness through refined microstructure and grain boundary strengthening via grain size reduction, i.e., Hall-Petch strengthening [5,6]. A recent example of an extrinsically superhard material is nanocrystalline *beta*-SiC, which has been demonstrated to have a ~60% increase in hardness over its intrinsic hardness when the average grain size is 9.9 nm [7]. Extrinsically superhard materials pose as highly attractive alternatives to expensive and challenging to manufacture intrinsically superhard materials.

1.2 Applications and Traditional Processing of Tungsten Carbide

Tungsten carbide (WC), ubiquitous in cutting tools and abrasives [8], is a promising candidate material for extrinsic superhardening. Pure (i.e. binderless) WC has Vickers hardness (*HV*) values typically near 26 GPa [9], which exceeds the performance of other common hard materials with similar applications such as SiC (~26 GPa [10,11]), and α-Al_2O_3 (< 21 GPa [12,13]). Furthermore, extrinsically superhardened WC would represent a unique material class considering its high density (15.63 g/cm^3) relative to all other known superhard materials, having densities below ~3.51 g/cm^3 (density of diamond), including the recent development of nanocrystalline *beta*-SiC. Nonetheless, despite the relative hardness of pure WC, an increase in hardness would be required to reach the hardness of intrinsically superhard materials. Such hardening necessitates significant microstructure refinement including a dramatic reduction in grain size.

Manuscript approved December 6, 2023.

However, the use of traditional approaches to sinter fully dense tungsten carbide with refined microstructure presents two major challenges. First, due to its high melting point (~2800°C) [14], production of fully dense binderless WC requires specialized high temperature furnaces. Common WC sintering processes add metallic binders such as Co (cemented carbides) to lower sintering temperature and improve densification at the expense of hardness (< 20 GPa) [15,16]. Typical hot pressing of cemented tungsten carbide is performed at >1300°C [17,18], while pure, binderless tungsten carbide requires >2000°C to achieve full density [19,20]. Secondly, high temperature sintering typically results in excessive grain growth which prevents refined microstructure formation. Thus, novel processing approaches are required to preserve nanoscale grain size while eliminating all porosity to maximize hardness.

1.3 Advanced Processing and Potential Superhardness for Tungsten Carbide

Recent advances in sintering technology have enabled lower temperature sintering of ceramics including tungsten carbide. These novel approaches result in smaller grain sizes and thus significant hardening. For example, the combination of applied pressure and rapid heating in spark plasma sintering (SPS) and high-frequency induction-heated sintering (HFIHS) have yielded dense binderless tungsten carbide with submicron grain sizes and increased hardness for ceramics sintered at temperatures ≤ 1500°C [21–23]. In particular, HFIHS at 1250°C under 80 MPa applied pressure was utilized to produce pure WC with near full density and grain sizes as small as 87 nm leading to a hardness of 30 GPa [24]. Through these advanced sintering techniques, extrinsic hardening of WC has been demonstrated through grain refinement. These efforts demonstrated the increase in hardness by reducing grain size in WC, yet the goal of reaching superhardness in WC still remains untapped.

The path to superhard WC requires significant additional hardening through mechanisms beyond grain size reduction. Lattice deformation presents a potential mechanism of extrinsic hardening through resultant intragranular barriers to dislocation movement such as nanotwins. Lattice deformation as a significant hardening mechanism in WC was observed by Zhang, et al. who reported submicron grain size pure WC produced through a high pressure assisted sintering approach (10 GPa applied pressure) with a surprising Vickers hardness of 33 GPa, 10% harder than previously reported much smaller grained nanocrystalline WC [24,25]. The unexpectedly high hardness was attributed to nanoscale intragranular substructures induced by the high applied pressure during sintering. Extraordinary hardening through lattice deformation has also been demonstrated in other superhard materials such nanotwinned cBN (108 GPa [26]) and nanotwinned diamond (> 200 GPa [27]). Based on the separate successes of grain size refinement and lattice deformation in the hardening of WC, the superposition of multiple hardening mechanisms is proposed as route to extrinsically superhardened WC. While interdependent hardening mechanisms have been modeled by others [28,29], the particular combined effects of grain size and intragranular substructures reported in this work are unique, especially with regards to the synthesis of novel extrinsically superhard materials.

In pursuit of fully dense, nanocrystalline WC with intragranular substructures, a sintering approach known as environmentally controlled - pressure assisted sintering (EC-PAS) was utilized in this work. EC-PAS has previously been applied to demonstrate the Hall-Petch relationship and unprecedented high hardness in nanocrystalline spinel ceramics [30,31]. In those experiments, fully dense $MgAl_2O_4$ spinel was produced with grain sizes as small as 3.6 nm using sintering pressures of 2 GPa and temperatures as low as 640°C [32]. This present work represents the first reported use of the EC-PAS process to sinter non-oxides, expanding its application to carbides. The EC-PAS process exploits a closed environment protected from ambient air and moisture throughout stages ranging from the heat treatment of nanopowders to green body compaction and sintering. This approach minimizes adsorbates that may reduce nanopowder surface energy and inhibit sintering. In conjunction with applied pressure, full

densification may be achieved at relatively low sintering temperatures (< 0.5 T_m), thus minimizing grain growth and preserving nanocrystallinity. Furthermore, this work demonstrates that applied pressures can also induce lattice deformations in WC leading to intragranular substructures and additional hardening.

2. EXPERIMENTAL APPROACH

2.1 Processing

Experiments included exploration of material processing in two broad steps: heat treatment of nanopowders and sintering of nanopowders.

2.1.1 Powder Preparation

Tungsten carbide nanopowder was obtained from Cerion Nanomaterials, LLC (Rochester, NY, USA). Using X-ray diffraction (XRD) and Brunauer, Emmett, and Teller (BET) surface area measurements [33], the powder was determined to be single phase WC (PDF Card 04-002-2679) with an average grain size of 20.3 nm and average particle size of 64 nm (surface area 6 m^2/g, density 15.63 g/cm^3). The powders were prepared for sintering through annealing in a fused quartz tube under 10% H_2 (balance Ar) flow at 450°C, 700°C, and 800°C for 12 hours in fused quartz boats to evaporate moisture and organics from the particle surfaces and reduce potential surface oxides present below the detection limit of XRD.

2.1.2 Sintering

Powders were then pressed in tungsten carbide dies at 393 MPa for 5 minutes, resulting in 12 mm diameter, 2 mm thick discs of approximately 50% relative density. The pressed WC discs were then hermetically sealed in metal capsules. Powders were not exposed to ambient conditions between annealing and sealing into the capsules by handling in an N_2 glove box. In preparation for sintering, the metal capsules were placed in partially sintered stabilized zirconia high pressure cells equipped with graphite heaters. The high pressure cells were then loaded into a split sphere design high pressure high temperature (HPHT) apparatus. Sintering was performed at 850°C, 1050°C, and 1200°C with a 15 minute soak under approximately 2 GPa quasi-hydrostatic applied pressure, with pressurization occurring prior to heating. Heating and cooling rates were 20°C and 50°C per minute, respectively. After sintering, samples were removed from high pressure cells and capsules, and polished to a mirror finish.

2.2 Characterization

Nanopowders and sintered bodies were microstructurally characterized including grain size, and grain structure, surface area, density, and nanostructure through TEM. Mechanical characterization of sintered bodies was conducted through indentation.

2.2.1 Grain Size, Density, and Microscopy

Grain size was determined using Halder-Wagner crystallite size analysis [34] in MDI Jade 9 software. Brunauer, Emmett, and Teller method surface area measurements were conducted with a Micromeritics ASAP 2020 Accelerated Surface Area and Porosimetry system. Density was evaluated through both He pycnometry using a Micromeritics AccuPyc II 1340 and image analysis of scanning electron microscopy (SEM) micrographs captured with a JEOL JSM-7001F SEM operated at 20 kV. High resolution transmission electron microscopy (HRTEM) was conducted on 2 sintered samples (26.1 nm, 53.9 nm grain sizes). Specimens were prepared for analysis by crushing part of sintered bodies into a

powder in an alcohol medium, followed by transfer to a carbon coated Cu grid. Analysis was performed using a JEOL 2200 analytical transmission electron microscope operating at 200 keV.

2.2.2 Indentation

Vickers microhardness was measured using a LECO AMH55 under a 1 kg load with a 15 second hold. Indentation fracture toughness was calculated using the Lankford Eq. (1),

$$K_{Ic} = 0.0782 \cdot \left(HV \cdot a^{1/2}\right) \cdot \left(\frac{E}{HV}\right)^{2/5} \cdot \left(\frac{c}{a}\right)^{-1.56} \quad (1)$$

after measuring crack lengths (c) and indent diagonals (a) using optical images captured at 40x magnification after indentation. Young's modulus, E, was assumed to be 690 GPa. The Lankford equation was selected due to its application to both median and Palmqvist type cracks [35]. Instrumented indentation was performed with a Hysitron Ubi-750 Nanoindenter with a Berkovich tip on the WC ceramics sintered at 1050°C. A 2N load was applied with a 2 second hold and 5 second loading and unloading periods, which produced indents approximately 2 µm deep. Hardness was calculated using the Oliver-Pharr method [36,37]. For all indentation, 16 indents were performed per specimen.

3. RESULTS

3.1 WC Nanopowders and Annealing

Powder annealing to remove surface adsorbates in preparation for sintering resulted in very limited coarsening at all temperatures. A maximum increase in grain size from 20.3 to 27.2 nm was accompanied by slight decomposition of WC to W (6.4 wt%) at 800°C as seen in Fig. 1, along with a scanning electron microscopy (SEM) micrograph of the pre-annealed powder. The effect of annealing temperature on powder grain size and composition may be seen in Table 1. Below 800°C only the WC phase was detected through X-ray diffraction (XRD). The decomposition of WC to W is consistent with past observations of decarburization of nanocrystalline WC powder during annealing at 800°C and above, which has been attributed to reactions with oxygen impurities especially prevalent in WC nanopowders due to their large surface area [38,39].

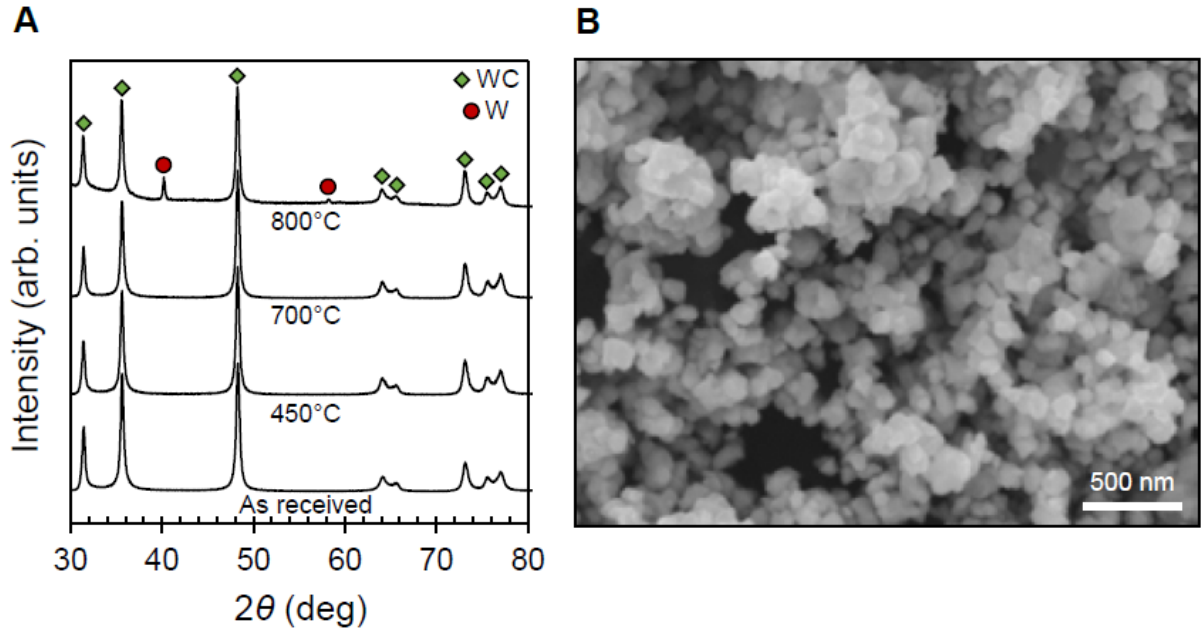

Fig. 1—WC nanopowders and annealing. a) XRD patterns from WC nanopowders before and after annealing under H_2 at 450°C, 700°C, and 800°C. Powders appear to be single phase WC below 800°C, at which temperature small amounts of W are observed. b) SEM micrograph of as received WC nanopowder.

Table 1—Effect of Annealing Temperature on WC Nanopowder Grain Size and Composition

Annealing Temperature (°C)	Average Grain Size (nm)		Composition (wt%)	
	WC	W	WC	W
As received	20.3		100	
450	22.2		100	
700	23.8		100	
800	27.2	67.2	93.6	6.4

The apparent absence of decarburization implies the presence of residual oxygen impurities in the powder annealed below 800°C. However, compositional and grain size differences between powders annealed at different temperatures did not appear to have any significant effect on the sintered bodies in terms of grain size, density, hardness, or fracture toughness. Despite compositional differences, it is assumed that the effect of the anneals on powder surfaces was similar at all temperatures, and that coarsening and WC decomposition were insignificant relative to sintering temperature in determining the properties of the sintered bodies.

3.2 WC Sintering: EC-PAS

All sintered WC specimens were determined to be single phase through X-ray diffraction as seen in Fig. 2a despite the compositional differences in the annealed powders. Small concentrations of second phases may exist below the detection limit of XRD (~1 vol %). The apparent W to WC phase

transformation in sintered bodies produced from powders with significant W content (annealed at 800°C) may indicate free carbon present in the annealed powder [40]. Decarburization resulting in residual carbon has been observed in thermally sprayed WC-12Co, processed with argon as primary gas [41]. An overview of sintered specimens and their measured mechanical properties may be found in Table 2.

Table 2—Properties of Sintered Tungsten Carbide Ceramics

Powder Annealing Temperature (°C)	Sintering Temperature (°C)	Relative Density (%)	Average Grain Size (nm)	*HV** (GPa)	Instrumented Indentation Hardness* (GPa)	Indentation Fracture Toughness* (MPa√m)
700	850	96	14.7	12.7 ± 0.9		8.1 ± 0.6
450	1050	99	26.1	37.1 ± 1.6	37.5 ± 0.6	6.7 ± 0.4
700	1050	100	27.7	38.8 ± 0.7	38.2 ± 0.3	9.4 ± 0.6
800	1050	99.1	27.5	37.9 ± 1.1	38.6 ± 0.3	8.8 ± 0.5
450	1200	99.4	49.3	37.2 ± 1.4		9.5 ± 0.8
700	1200	99.9	52.0	35.6 ± 3.1		6.2 ± 0.6
800	1200	100	53.9	36.4 ± 2.3		8.4 ± 0.5

*± 1 standard deviation

Both grain size and density of the sintered specimens were observed to increase with sintering temperature as seen in Fig. 2b. Relative density increased from ~96% at 850°C to >99% at 1050°C and 1200°C. At 850°C, grain size was observed to be smaller than that in the initial powder (14.7 nm vs 23.8 nm), suggest fracturing of WC powder during pressurization to 2 GPa. Grain size increased slightly at 1050°C (from 22-27 nm to 26-28 nm), and more significantly at 1200°C (49-54 nm). Based on grain size and density, the optimum sintering temperature appears to be near 1050°C, which also yielded the highest hardnesses.

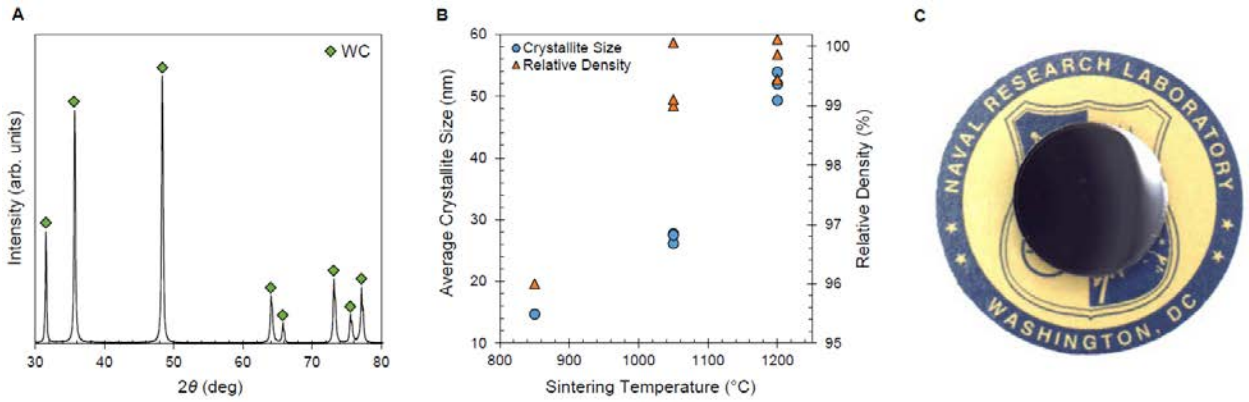

Fig. 2—WC sintering. a) Representative XRD pattern from sintered WC demonstrating single phase composition. b) Crystallite size and density of sintered WC versus sintering temperature. c) Photograph of WC specimen, HV = 38.8 ± 0.7 GPa, average grain size = 27.7 nm, sintered at 1050°C from WC nanopowder annealed at 700°C.

3.3 WC Mechanical Properties

Vickers hardnesses of up to 39 GPa were measured in the binderless nanocrystalline tungsten carbide ceramics (Fig. 3a and Table 2). This represents a 18% increase over the previously reported maximum hardness in pure WC, 33 GPa [25], and an even larger 30% increase over all other reported hardnesses (second highest, 30 GPa) [24,42]. The highest Vickers hardness (38.8 ± 0.7 GPa) in this study was recorded in a specimen with an average grain size of 27.7 nm sintered at 1050°C from WC nanopowder annealed at 700°C. Vickers microindentation results were confirmed through instrumented indentation on a subset of samples. As seen in Fig. 3a, nearly identical hardness values were obtained through Vickers microindentation and instrumented indentation. The consistency in measured hardness despite the range of applied indentation load suggests a negligible indentation size effect in the load range used in this study (2 – 10 N). Much lower hardnesses were measured in the smallest grained sample (14.7 nm) that had been sintered at 850°C, suggesting incomplete sintering also supported by the apparent lack of densification. A slight drop in hardness to 36-37 GPa was observed in larger grained samples, which may be attributed to the Hall-Petch effect.

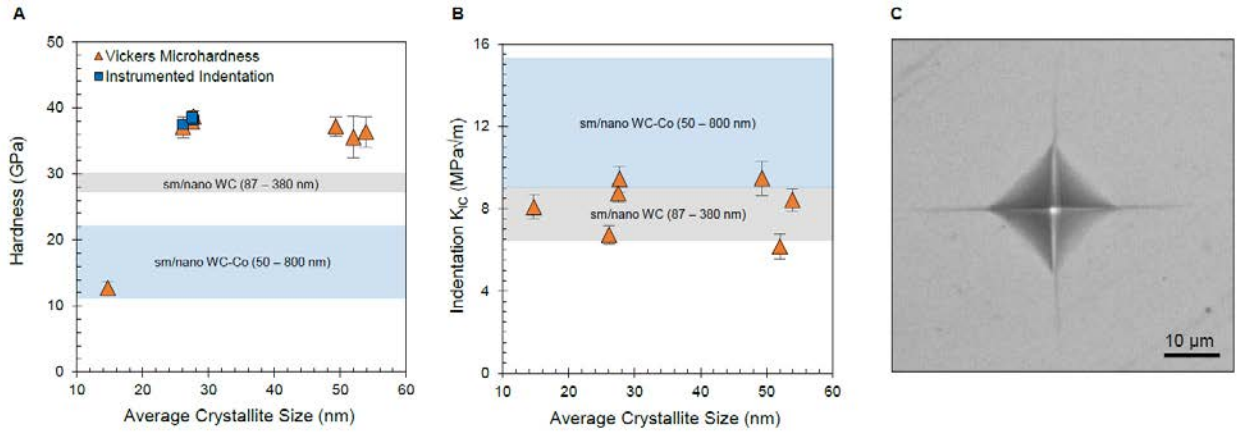

Fig. 3—WC mechanical properties. a) Hardness and b) indentation fracture toughness plotted against average crystallite size as determined through Vickers microindentation and instrumented indentation. Results are compared to typical literature values [15,43] for similar materials (submicron (sm) and nanograined (nano) WC and WC-Co) without respect to grain size. Data points represent average values with standard deviation error bars (n = 16). c) Optical micrograph of representative indent from Vickers microindentation.

Indentation fracture toughness was found to be independent of grain size, ranging from 6.2 to 9.5 MPa√m. Despite the generally accepted tradeoff between hardness and fracture toughness, which is observed in larger grained pure WC, this relationship diminishes as grain sizes approach the nanocrystalline regime in pure WC [43,44]. As seen in Fig. 3b, this range compares favorably to indentation fracture toughness values from the literature for pure WC, though falls short of values recorded for WC-Co as expected based on the toughening effect of the metallic binder [15,43]. The toughness measured in this study however is significantly below the value of 13.7 MPa√m that reported by Zhang et al. (albeit in a presumably coarser grained pure WC sintered at 1500°C with a hardness of 21 GPa) [25].

3.4 Lattice Deformation and Intragranular Substructures

High resolution transmission electron microscopy (HRTEM) imaging of WC revealed a highly deformed microstructure consisting of nanoscale substructures within grains similar to subgrains. Samples sintered at 1050°C (26.1 nm grain size) and 1200°C (53.9 nm grain size) were imaged, but no

significant differences in the grain substructure were observed. Fig. 4 and 5 features HRTEM images, Fast Fourier Transform (FFT) patterns from these images, and the filtered images resulting from Inverse Fast Fourier Transform. In Fig. 4, prismatic plane twin reflections can be seen (red circles) in the FFT patterns, which correspond with twins indicated by red brackets in the IFFT images. The high density of twins results in substructures typically 2-3 nm wide. Fig. 4a and 4b exhibit lattice deformation parallel to the basal plane as well, manifesting in lattice bending. The resultant lattice bending can be more clearly observed in Fig. 5, particularly in the approximately 15° rotation of the FFT pattern. Lattice bending and resulting substructures (in red brackets) can be clearly seen in Fig. 5c, along with dislocations indicated by white arrows.

The significant deformation, characterized by widespread nanotwins is likely a plastic response to the applied 2 GPa pressure before and during sintering. WC is known to undergo plastic deformation, especially at elevated temperature [45,46]. Nanotwins in highly deformed material have been observed in high pressure sintering studies of WC [25,44], and similar materials such as TaC [47]. Zhang et al. observed similar nanotwins in WC sintered at 10 GPa, and attributed the anomalously high measured hardness to these defects [25].

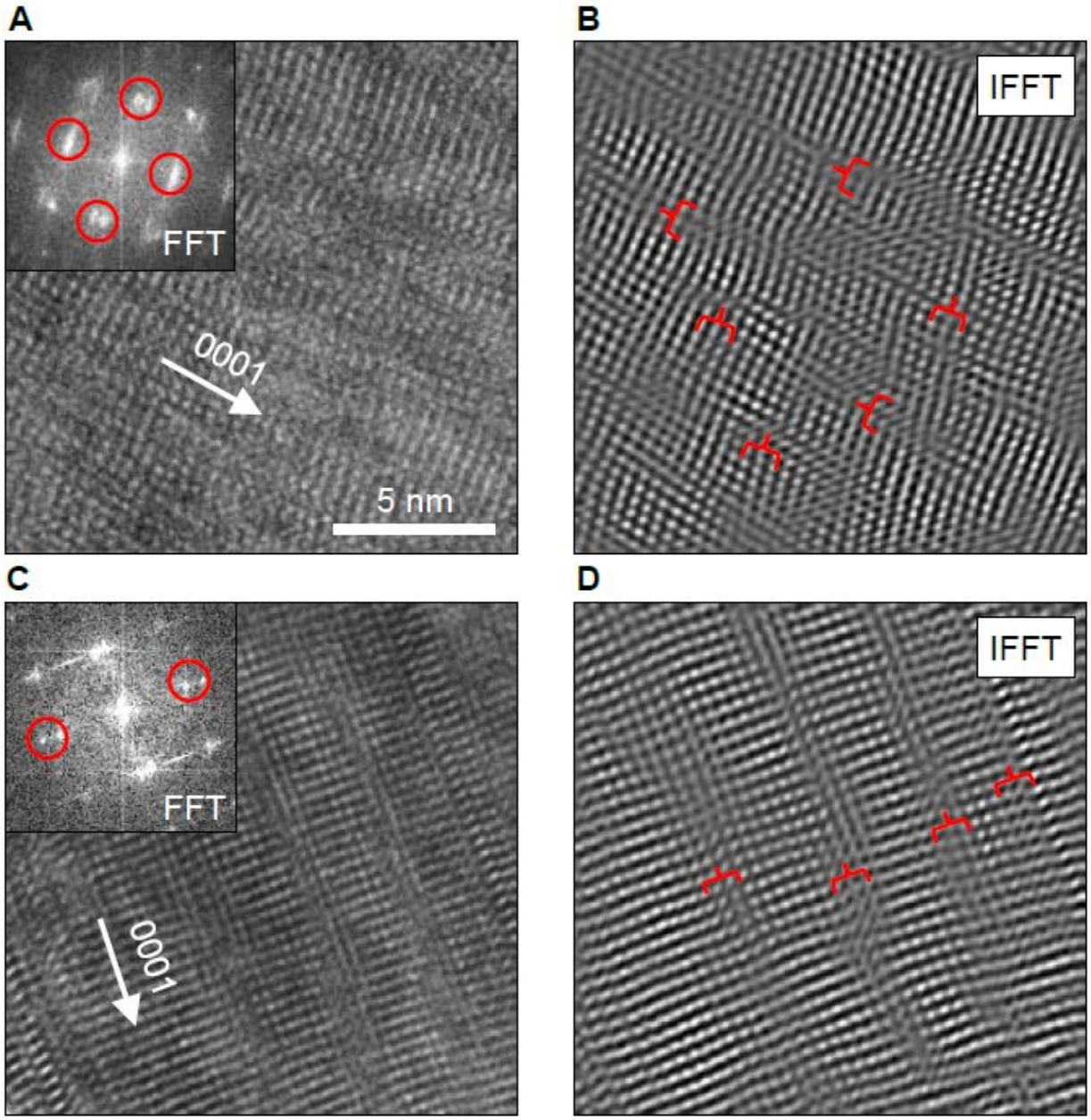

Fig. 4—Lattice deformations including bending and nanotwinning in WC. HRTEM micrographs (a, c) of WC sintered at 1050°C, along with Fast Fourier Transform (FFT) diffraction patterns (insets) and Inverse Fast Fourier Transform (IFFT) images (b, d) from the same region. Red circles highlight twinned reflections in FFT diffraction patterns which correspond with red brackets indicating twinned regions in the IFFT images.

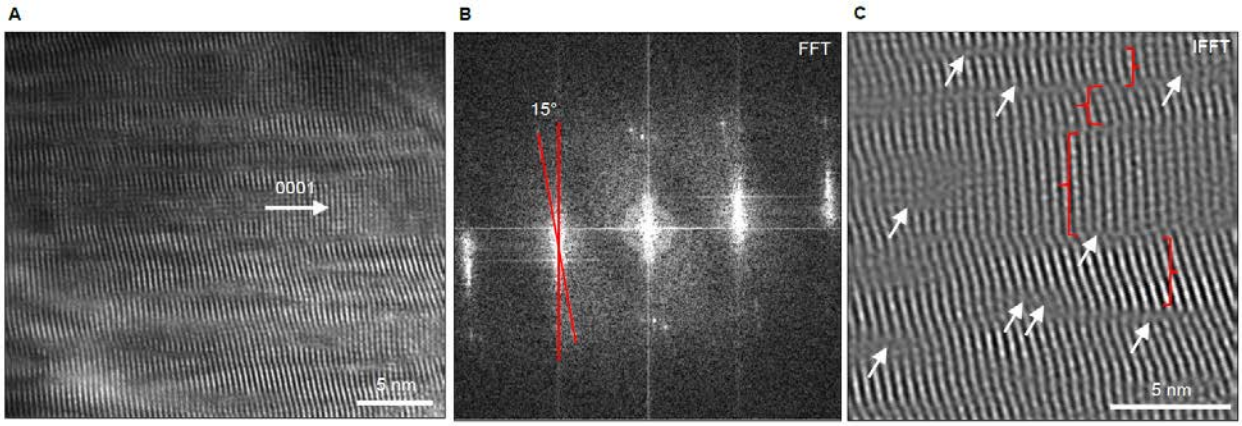

Fig. 5—Lattice deformation and intragranular substructures in WC. a) HRTEM micrograph of WC sintered at 1050°C exhibiting lattice deformation. b) Fast Fourier Transform (FFT) diffraction pattern from same region demonstrating 15° lattice rotation resulting from lattice deformation. c) Inverse Fast Fourier Transform (IFFT) image from part of a) with white arrows indicating dislocations and red brackets indicating substructures, both resulting from lattice deformation.

4. DISCUSSION

4.1 Near Superhardness

The hardness of the nanocrystalline tungsten carbide can be attributed to the small grain size, high density, and intragranular substructure resulting from enhanced sintering during EC-PAS. Two parameters distinguish the approach in this work from previous studies. Firstly, the applied pressure of 2 GPa is greater than most pure WC sintering studies to date. Only 2 studies were found that utilized higher pressures, including 5 GPa (at 1100 - 1600°C) [44] and 10 GPa (1000 – 1500°C) [25]. In these studies, extremely high applied pressures resulted in high density and limited grain growth. However, significantly larger grain sizes (submicron) and lower hardnesses (maximum 29 and 33 GPa, respectively) were observed relative to this work despite much higher applied pressures. In part, the larger grain sizes resulted from larger grained starting powder (~200 nm grain size in both studies). Based on the higher sintering temperatures required for densification in these works however, it is possible significant grain growth would have been observed with finer powders. Secondly, and potentially more significantly, the approach in this study is the first to feature isolation of nanopowder surfaces from ambient conditions between powder drying/annealing and sintering. This approach is expected to result in significantly higher surface energies due to the prevention of moisture and oxygen adsorption. The use of finer nanopowder in combination with the maximization of powder surface energy through the EC-PAS approach permitted full densification at lower sintering temperatures relative to these studies, with maximum hardness achieved at 1050°C as opposed to 1500°C [44] and 1300°C [25].

In addition to grain size effects, the extensive lattice deformation observed through HRTEM in this work may contribute to additional hardening by creating additional slip barriers. Hardening effects beyond grain size refinement have been reported for both metal and ceramics through the effects of nanotwins [48–50] and, importantly, Zhang et al. [25] also attribute their abnormally high hardness in WC to be due in part to the numerous stacking faults and twin defects present within the submicron grain structure.

4.2 Superposition of Hardening Mechanisms

To evaluate the role of grain size and nanoscale lattice deformation substructures in hardening, hardness data from this study along with submicron and nanocrystalline pure WC hardness data from literature [25,43] were plotted against the inverse square root of grain size as seen in Fig. 6. All data points represent samples with 99% relative density or greater. The distribution of hardness data suggests the possibility of two linear regimes, offset but with similar slopes. A linear fit can be captured via the Hall-Petch Eq. (2), which represents the historically observed inverse relationship between grain size and yield strength or hardness, and has been well characterized for a variety of materials [5,6].

$$H_V = H_0 + \sqrt{\frac{k}{d}} \tag{2}$$

HV is the Vickers hardness (GPa), H0 is the Vickers hardness of a WC single crystal (GPa), k is a fitting parameter, and d is the average grain size (nm). Through linear regression, the Hall-Petch equation was first applied to the lower hardness regime, which consists of relatively consistent literature data < 30 GPa [43] (dashed line). This fit yields the Hall-Petch constants H0 = 25.4 GPa and k = 1656. This H0 value is consistent with single crystal hardness measurements from literature [9].

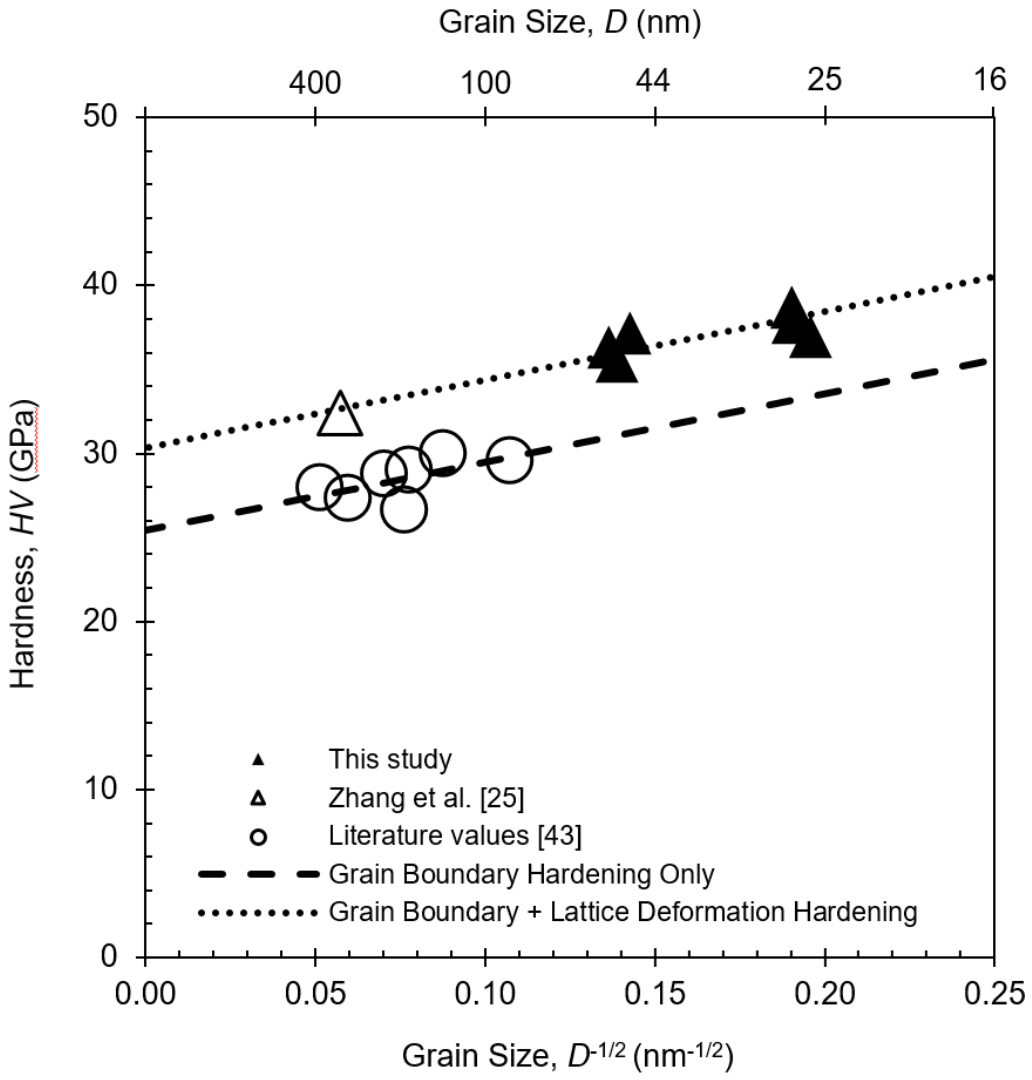

Fig. 6—Superposition of hardening mechanisms in WC. Hardness plotted against inverse grain size including data from this study and literature values, with linear regression applied to two apparent regimes.

The apparent higher hardness regime includes data from this study and a single outlier literature data point at 33 GPa [25]. The extensive lattice deformation observed in Fig. 4 and 5 suggests a potential physical basis for this regime, as Zhang et al also characterized an intragranular defect structure [25]. Just as grain size refinement leads to hardening by limiting the mean free path length for dislocation motion and propagation, intragranular lattice deformations and defects may also pin dislocation motion and lead to additional hardening. Based on this reasoning, the lower hardness regime is treated as the result of exclusively grain size effects ("Grain Boundary Hardening Only"), while the higher hardness regime is treated as a sum, or superposition, of grain size effects and a secondary size effect arising from lattice deformation ("Grain Boundary + Lattice Deformation Hardening"). Therefore, a modified Hall-Petch Eq. (3), may be applied to the high hardness regime. In Fig. 6, the higher hardness regime was fit with a linear regression based on Eq. (3) (dotted line), while retaining the values for k and H0 derived from fitting the lower hardness regime.

$$H_V = (H_0 + H_L) + \sqrt{\frac{k}{d}} \quad (3)$$

In this modified equation, an additional term is added to capture the apparent offset of the higher hardness regime. The constant HL is analogous to H0 as both constants represent materials properties driven by dislocation movement resistance, with HL representing the macroscopic effect of nanoscale lattice substructures on dislocations. Based on Eq. (3) and the linear fit of the higher hardness regime, HL was calculated to be 4.92 GPa. This analysis suggests 5 GPa of hardening may be attained through lattice substructuring alone in these WC ceramics. For the specimens produced in this work, 5 GPa represents 40 – 50% of the total hardening observed relative to typical WC. Significant variability in substructure size or periodicity was not observed in this work. Substructure size may have an effect on dislocation disruption, but currently there is a lack of data to explore this concept.

With regards to size effects, an alternative explanation for the observed regimes is that that lattice substructures behave similarly to grain boundaries, and the higher hardnesses are solely dependent on the substructure scale. However, fitting the maximum hardnesses measured in this study (39 GPa) to the "Grain Boundary Hardening Only" fit (dashed line in Fig. 6) yields an equivalent grain size of 9 nm, significantly larger than the observed lattice substructures (2-3 nm). The clear relationship between grain size and hardness in the higher hardness regime also supports the concept of superposition of multiple hardening mechanisms as opposed to an overwhelming lattice substructure effect.

5. CONCLUSIONS

In conclusion, environmentally controlled - pressure assisted sintering (EC-PAS) was utilized to produce fully dense, nanocrystalline (as small as 26 nm average grain size) binderless tungsten carbide with near superhard hardness (39 GPa), a significant leap in both hardness (previously recorded maximum of 33 GPa [25]) and grain size (previously recorded minimum of 87 nm [44]). In addition to significantly increased hardness and reduced grain size, fracture toughness as measured through indentation (up to 9.5 MPa$\sqrt{m}$) remained comparable to other reports for submicron and nanocrystalline WC. Maximization of surface energy and applied pressure (2 GPa) through the EC-PAS approach, in conjunction with nanocrystalline WC starting powder (20 nm grain size) permitted full densification at relatively low sintering temperatures ($\leq$ 1200°C), leading to minimal grain growth and nanocrystalline bulk material, very nearly elevating WC to superhard status. TEM observation revealed a highly deformed WC microstructure characterized by 2-3 nm substructures resulting from nanotwinning and lattice bending. This processing induced deformation may contribute to hardening through disruption of dislocation movement, and can be modeled as an additional constant in the Hall-Petch equation, HL. The combined hardening effects of nanocrystallinity and lattice deformation induced intragranular substructure represents a pathway to produce extrinsically superhard WC, and may be applied to other hard materials to further expand the class of superhard materials.

REFERENCES

1. H. Li, R.C. Bradt, The indentation size effect and the hardness of single crystal diamond on the (001)〈110〉, Diamond and Related Materials. 1 (1992) 1161–1167. https://doi.org/10.1016/0925-9635(92)90090-B.

2. Q. Liang, C. Yan, Y. Meng, J. Lai, S. Krasnicki, H. Mao, R.J. Hemley, Enhancing the mechanical properties of single-crystal CVD diamond, J. Phys.: Condens. Matter. 21 (2009) 364215. https://doi.org/10.1088/0953-8984/21/36/364215.

3. S. Dub, P. Lytvyn, V. Strelchuk, A. Nikolenko, Y. Stubrov, I. Petrusha, T. Taniguchi, S. Ivakhnenko, Vickers Hardness of Diamond and cBN Single Crystals: AFM Approach, Crystals. 7 (2017) 369. https://doi.org/10.3390/cryst7120369.

4. H. Sumiya, S. Uesaka, S. Satoh, Mechanical properties of high purity polycrystalline cBN synthesized by direct conversion sintering method, Journal of Materials Science. 35 (2000) 1181–1186. https://doi.org/10.1023/A:1004780218732.

5. E.O. Hall, The Deformation and Ageing of Mild Steel: III Discussion of Results, Proc. Phys. Soc. B. 64 (1951) 747–753. https://doi.org/10.1088/0370-1301/64/9/303.

6. N.J. Petch, The Cleavage Strength of Polycrystals, Journal of the Iron and Steel Institute. 174 (1953) 25–28.

7. R. Sun, X. Wei, W. Hu, P. Ying, Y. Wu, L. Wang, S. Chen, X. Zhang, M. Ma, D. Yu, L. Wang, G. Gao, B. Xu, Y. Tian, Nanocrystalline Cubic Silicon Carbide: A Route to Superhardness, Small. 18 (2022) 2201212. https://doi.org/10.1002/smll.202201212.

8. L.J. Prakash, Application of fine grained tungsten carbide based cemented carbides, International Journal of Refractory Metals and Hard Materials. 13 (1995) 257–264. https://doi.org/10.1016/0263-4368(95)92672-7.

9. J.J. Roa, E. Jimenez-Pique, C. Verge, J.M. Tarragó, A. Mateo, J. Fair, L. Llanes, Intrinsic hardness of constitutive phases in WC–Co composites: Nanoindentation testing, statistical analysis, WC crystal orientation effects and flow stress for the constrained metallic binder, Journal of the European Ceramic Society. 35 (2015) 3419–3425. https://doi.org/10.1016/j.jeurceramsoc.2015.04.021.

10. L. Vargas-Gonzalez, R.F. Speyer, J. Campbell, Flexural Strength, Fracture Toughness, and Hardness of Silicon Carbide and Boron Carbide Armor Ceramics, International Journal of Applied Ceramic Technology. 7 (2010) 643–651. https://doi.org/10.1111/j.1744-7402.2010.02501.x.

11. Yu.V. Milman, S.I. Chugunova, I.V. Goncharova, T. Chudoba, W. Lojkowski, W. Gooch, Temperature dependence of hardness in silicon–carbide ceramics with different porosity, International Journal of Refractory Metals and Hard Materials. 17 (1999) 361–368. https://doi.org/10.1016/S0263-4368(99)00022-0.

12. A. Krell, A new look at the influences of load, grain size and grain boundaries on the room temperature hardness of ceramics, International Journal of Refractory Metals and Hard Materials. 16 (1998) 331–335. https://doi.org/10.1016/S0263-4368(98)00056-0.

13. M. Munro, Evaluated Material Properties for a Sintered alpha-Alumina, Journal of the American Ceramic Society. 80 (1997) 1919–1928. https://doi.org/10.1111/j.1151-2916.1997.tb03074.x.

14. R.P. Pohanish, Sittig's Handbook of Toxic and Hazardous Chemicals and Carcinogens, William Andrew, 2011.

15. Z.Z. Fang, X. Wang, T. Ryu, K.S. Hwang, H.Y. Sohn, Synthesis, sintering, and mechanical properties of nanocrystalline cemented tungsten carbide – A review, International Journal of Refractory Metals and Hard Materials. 27 (2009) 288–299. https://doi.org/10.1016/j.ijrmhm.2008.07.011.

16. G.S. Upadhyaya, Materials science of cemented carbides — an overview, Materials & Design. 22 (2001) 483–489. https://doi.org/10.1016/S0261-3069(01)00007-3.

17. L. Sun, C.-C. Jia, M. Xian, A research on the grain growth of WC–Co cemented carbide, International Journal of Refractory Metals and Hard Materials. 25 (2007) 121–124. https://doi.org/10.1016/j.ijrmhm.2006.03.002.

18. M.S. El-Eskandarany, A.A. Mahday, H.A. Ahmed, A.H. Amer, Synthesis and characterizations of ball-milled nanocrystalline WC and nanocomposite WC–Co powders and subsequent consolidations, Journal of Alloys and Compounds. 312 (2000) 315–325. https://doi.org/10.1016/S0925-8388(00)01155-5.

19. A. Gubernat, P. Rutkowski, G. Grabowski, D. Zientara, Hot pressing of tungsten carbide with and without sintering additives, International Journal of Refractory Metals and Hard Materials. 43 (2014) 193–199. https://doi.org/10.1016/j.ijrmhm.2013.12.002.

20. Y. Wang, D. Zhu, X. Jiang, P. Sun, Binderless sub-micron WC consolidated by hot pressing and treated by hot isostatic pressing, Journal of the Ceramic Society of Japan. 122 (2014) 329–335. https://doi.org/10.2109/jcersj2.122.329.

21. B. Huang, L.D. Chen, S.Q. Bai, Bulk ultrafine binderless WC prepared by spark plasma sintering, Scripta Materialia. 54 (2006) 441–445. https://doi.org/10.1016/j.scriptamat.2005.10.014.

22. J. Zhang, G. Zhang, S. Zhao, X. Song, Binder-free WC bulk synthesized by spark plasma sintering, Journal of Alloys and Compounds. 479 (2009) 427–431. https://doi.org/10.1016/j.jallcom.2008.12.151.

23. H.-C. Kim, I.-J. Shon, I.-K. Jeong, I.-Y. Ko, J.-K. Yoon, J.-M. Doh, Rapid sintering of ultra fine WC and WC-Co hard materials by high-frequency induction heated sintering and their mechanical properties, Met. Mater. Int. 13 (2007) 39–45. https://doi.org/10.1007/BF03027821.

24. I.-J. Shon, B.-R. Kim, J.-M. Doh, J.-K. Yoon, K.-D. Woo, Properties and rapid consolidation of ultra-hard tungsten carbide, Journal of Alloys and Compounds. 489 (2010) L4–L8. https://doi.org/10.1016/j.jallcom.2009.09.040.

25. Y. Zhang, Z. Kou, Z. Wang, M. Yang, J. Lu, H. Liang, S. Guan, Q. Hu, H. Gong, D. He, Magic high-pressure strengthening in tungsten carbide system, Ceramics International. 45 (2019) 8721–8726. https://doi.org/10.1016/j.ceramint.2019.01.195.

26. Y. Tian, B. Xu, D. Yu, Y. Ma, Y. Wang, Y. Jiang, W. Hu, C. Tang, Y. Gao, K. Luo, Z. Zhao, L.-M. Wang, B. Wen, J. He, Z. Liu, Ultrahard nanotwinned cubic boron nitride, Nature. 493 (2013) 385–388. https://doi.org/10.1038/nature11728.

27. Q. Huang, D. Yu, B. Xu, W. Hu, Y. Ma, Y. Wang, Z. Zhao, B. Wen, J. He, Z. Liu, Y. Tian, Nanotwinned diamond with unprecedented hardness and stability, Nature. 510 (2014) 250–253. https://doi.org/10.1038/nature13381.

28. X. Hou, N.M. Jennett, Application of a modified slip-distance theory to the indentation of single-crystal and polycrystalline copper to model the interactions between indentation size and structure size effects, Acta Materialia. 60 (2012) 4128–4135. https://doi.org/10.1016/j.actamat.2012.03.054.

29. X. Hou, N.M. Jennett, M. Parlinska-Wojtan, Exploiting interactions between structure size and indentation size effects to determine the characteristic dimension of nano-structured materials by indentation, J. Phys. D: Appl. Phys. 46 (2013) 265301. https://doi.org/10.1088/0022-3727/46/26/265301.

30. J.A. Wollmershauser, B.N. Feigelson, E.P. Gorzkowski, C.T. Ellis, R. Goswami, S.B. Qadri, J.G. Tischler, F.J. Kub, R.K. Everett, An extended hardness limit in bulk nanoceramics, Acta Materialia. 69 (2014) 9–16. https://doi.org/10.1016/j.actamat.2014.01.030.

31. J.A. Wollmershauser, B.N. Feigelson, E.P. Gorzkowski, C.T. Ellis, R. Goswami, S.B. Qadri, D.D. Nguyen, J.G. Tischler, F.J. Kub, R.K. Everett, Reply to comments on “An extended hardness limit in bulk nanoceramics”, Acta Materialia 69 (2014) 9–16, Scripta Materialia. 92 (2014) 65–68. https://doi.org/10.1016/j.scriptamat.2014.08.016.

32. H. Ryou, J.W. Drazin, K.J. Wahl, S.B. Qadri, E.P. Gorzkowski, B.N. Feigelson, J.A. Wollmershauser, Below the Hall–Petch Limit in Nanocrystalline Ceramics, ACS Nano. 12 (2018) 3083–3094. https://doi.org/10.1021/acsnano.7b07380.

33. . Brunauer, P.H. Emmett, E. Teller, Adsorption of Gases in Multimolecular Layers, J. Am. Chem. Soc. 60 (1938) 309–319. https://doi.org/10.1021/ja01269a023.

34. N.C. Halder, C.N.J. Wagner, Separation of particle size and lattice strain in integral breadth measurements, Acta Cryst. 20 (1966) 312–313. https://doi.org/10.1107/S0365110X66000628.

35. J. Lankford, Indentation microfracture in the Palmqvist crack regime: implications for fracture toughness evaluation by the indentation method, J Mater Sci Lett. 1 (1982) 493–495. https://doi.org/10.1007/BF00721938.

36. W. Oliver, G.M. Pharr, Measurement of hardness and elastic modulus by instrumented indentation, J. Mater. Res. 19 (2004).

37. W.C. Oliver, G.M. Pharr, An improved technique for determining hardness and elastic modulus using load and displacement sensing indentation experiments, Journal of Materials Research. 7 (1992) 1564–1583. https://doi.org/10.1557/JMR.1992.1564.

38. A.S. Kurlov, A.I. Gusev, Peculiarities of vacuum annealing of nanocrystalline WC powders, International Journal of Refractory Metals and Hard Materials. 32 (2012) 51–60. https://doi.org/10.1016/j.ijrmhm.2012.01.009.

39. A.S. Kurlov, A.I. Gusev, Vacuum annealing of nanocrystalline WC powders, Inorg Mater. 48 (2012) 680–690. https://doi.org/10.1134/S0020168512060088.

40. A.S. Kurlov, A.I. Gusev, Tungsten carbides and W-C phase diagram, Inorg Mater. 42 (2006) 121–127. https://doi.org/10.1134/S0020168506020051.

41. J. Nerz, B. Kushner, A. Rotolico, Microstructural evaluation of tungsten carbide-cobalt coatings, JTST. 1 (1992) 147–152. https://doi.org/10.1007/BF02659015.

42. M. Dopita, C. Rajagopalan, D. Chmelik, A. Salomon, H. Seifert, SPARK PLASMA SINTERING OF NANOCRYSTALLINE BINDERLESS WC HARD METALS, 10 (2010).

43. J. Sun, J. Zhao, Z. Huang, K. Yan, X. Shen, J. Xing, Y. Gao, Y. Jian, H. Yang, B. Li, A Review on Binderless Tungsten Carbide: Development and Application, Nano-Micro Lett. 12 (2019) 13. https://doi.org/10.1007/s40820-019-0346-1.

44. D. Ma, Z. Kou, Y. Liu, Y. Wang, S. Gao, X. Luo, W. Li, Y. Wang, Y. Du, L. Lei, Sub-micron binderless tungsten carbide sintering behavior under high pressure and high temperature, International Journal of Refractory Metals and Hard Materials. 54 (2016) 427–432. https://doi.org/10.1016/j.ijrmhm.2015.10.001.

45. H. Jones, V. Tong, R. Ramachandramoorthy, K. Mingard, J. Michler, M. Gee, Micropillar compression of single crystal tungsten carbide, Part 1: Temperature and orientation dependence of deformation behaviour, International Journal of Refractory Metals and Hard Materials. 102 (2022) 105729. https://doi.org/10.1016/j.ijrmhm.2021.105729.

46. V. Tong, H. Jones, K. Mingard, Micropillar compression of single crystal tungsten carbide, part 2: Lattice rotation axis to identify deformation slip mechanisms, International Journal of Refractory Metals and Hard Materials. 103 (2022) 105734. https://doi.org/10.1016/j.ijrmhm.2021.105734.

47. D. Lahiri, V. Singh, G.R. Rodrigues, T.M.H. Costa, M.R. Gallas, S.R. Bakshi, S. Seal, A. Agarwal, Ultrahigh-pressure consolidation and deformation of tantalum carbide at ambient and high temperatures, Acta Materialia. 61 (2013) 4001–4009. https://doi.org/10.1016/j.actamat.2013.03.014.

48. Y. Wei, Y. Li, L. Zhu, Y. Liu, X. Lei, G. Wang, Y. Wu, Z. Mi, J. Liu, H. Wang, H. Gao, Evading the strength–ductility trade-off dilemma in steel through gradient hierarchical nanotwins, Nat Commun. 5 (2014) 3580. https://doi.org/10.1038/ncomms4580.

49. P. Ying, Y. Gao, B. Zhang, Y. Wu, G. Gao, P. Li, Z. Li, B. Xu, W. Hu, Z. Zhao, J. He, D. Yu, Y. Tian, High-Pressure Synthesis of cBN Nanoparticles with High-Density Nanotwin Substructures, ACS Omega. 5 (2020) 650–654. https://doi.org/10.1021/acsomega.9b03239.

50. Y. Zhang, N.R. Tao, K. Lu, Mechanical properties and rolling behaviors of nano-grained copper with embedded nano-twin bundles, Acta Materialia. 56 (2008) 2429–2440. https://doi.org/10.1016/j.actamat.2008.01.030.